Combining strong-motion, InSAR and GPS data to refine the fault geometry and source kinematics of the 2011, Mw 6.2, Christchurch earthquake (New Zealand),

E.M. Toraldo-Serra, B. Delouis, A. Emolo, A. Zollo

Geophysical Journal International

Geophys. J. Int. (2013) **194,** 1760–1777
Advance Access publication 2013 June 8

doi: 10.1093/gji/ggt186

Combining strong-motion, InSAR and GPS data to refine the fault geometry and source kinematics of the 2011, M_w 6.2, Christchurch earthquake (New Zealand)

Eugenio Maria Toraldo Serra,[1] Bertrand Delouis,[2] Antonio Emolo[1] and Aldo Zollo[1]

[1] *University of Naples Federico II, Italy. E-mail: toraldo@na.infn.it*
[2] *Géoazur, Université de Nice Sophia-Antipolis, Observatoire de la Côte d'Azur,* 250 *rue Albert Einstein, Valbonne* 06560, *France*

Accepted 2013 May 7. Received 2013 April 15; in original form 2012 September 27

SUMMARY

The space–time distribution of coseismic slip of the 2011 February 21, M_w 6.2, Christchurch earthquake, New Zealand, is explored, differently from all previous studies, through a joint inversion of geodetic and strong-motion data. The geodetic data consist of both global position system (GPS), from campaign and continuous stations, and synthetic aperture radar (SAR) interferograms from two ascending satellite tracks. The strong motion data consist of 10 stations located in the Canterbury plains, these stations offering a good azimuthal coverage of the event.

The kinematic rupture model for the analysed event was obtained using the parametrization and non-linear inversion scheme proposed by Delouis *et al.* In particular, for any subfault we explore for the local source time function (local slip history), slip direction and rupture onset time. The geometry of the fault plane used for the kinematic inversion is inferred from the analysis of the geodetic data. To validate our results we perform a resolution study for both the single and complete data sets, and an errors analysis of our final kinematic rupture model.

Considering the complexity highlighted by superficial deformation data, we adopted a fault model consisting of two partially overlapping segments, with dimensions 15 × 11 and 7 × 7 km^2, corresponding to different faulting types. This two-fault model, instead of single-fault model, is needed to reconstruct the complex shape of the superficial deformation data. The total seismic moment resulting from the joint inversion is 3.0 × 1025 dyne · cm ($M_w = 6.2$) with an average rupture velocity of 2.0 km s^{-1}.

Key words: Earthquake source observations; Seismicity and tectonics; Computational seismology.

INTRODUCTION

On 2011 February 21 at 23:51 (UTC time), the M_w 6.2 Christchurch earthquake occurred near (just 7 km southeast) the centre of the city of Christchurch, the second largest city in New Zealand, on the south island. The best-double couple focal mechanism for the event initially indicates oblique slip (59/59/147, strike/dip/rake GCMT). However, the full moment tensor solution contains a large degree of non-double couple motion pointing to source complexity. Extremely high accelerations (as 2.2 × g) were recorded near the epicentre area (Kaiser *et al.* 2012). Additionally, this event caused soil liquefaction, landslides, large rockfalls and a widespread damage to buildings of Christchurch (the damage was valued at about US$ 12–16 billion), and, tragically, 185 confirmed fatalities. The Christchurch earthquake occurred just 6 months after the 2010 September 4, M_w 7.1 Darfield earthquake, which broke the previously unknown Greendale fault in the west area of the Canterbury plains.

For the Christchurch earthquake, different fault geometries and source models for the slip and rupture velocity distributions are available in literature (Barnhart *et al.* 2011; Beavan *et al.* 2011, 2012; Holden 2011; Atzori *et al.* 2012; Elliott *et al.* 2012). In particular, in these works authors proposed both simple (one-fault plane; Barnhart *et al.* 2011; Beavan *et al.* 2011; Holden 2011) and complex (two- or more fault planes; Atzori *et al.* 2012; Beavan *et al.* 2012; Elliott *et al.* 2012) fault geometry solutions. These geometries were inferred analysing GPS data and aftershocks distribution (Barnhart *et al.* 2011; Beavan *et al.* 2011) and different InSAR data sets (Atzori *et al.* 2012; Beavan *et al.* 2012; Elliott *et al.* 2012). On the other hand, the large complexity of the coseismic surface displacement close to the epicentral area (around

Christchurch city), deriving from both GPS and InSAR data, indeed seems to suggest that a complex fault geometry with two- or more fault planes is more realistic than a model with a single plane.

The aim of this study is to investigate the fault geometry of the Christchurch earthquake from the analysis of the GPS and InSAR data sets and then to derive a kinematic source model from the joint inversion of all the available strong-motion, GPS and InSAR data sets, through the non-linear inversion method based on the simulated annealing algorithm developed by Delouis *et al.* (2002). Preliminarily, as explained in the following, we performed a selection of the available deformation data combining GPS and SAR observations in order to find a model able to explain the complex geometry of the coseismic displacement data. No kinematic rupture models for the 20111 February 21 Christchurch earthquake have been proposed in the previous studies (Beavan *et al.* 2011, 2012; Holden 2011; Atzori *et al.* 2012; Barnhart *et al.* 2011; Elliott *et al.* 2012) combining strong-motion, InSAR and GPS data in a joint inversion.

Tectonic and geological setting of the Canterbury plains

Seismicity in New Zealand is associated with the movements related to the boundary of the Pacific and Australian plates (40 mm yr^{-1}). The regional tectonics is dominated by three major structure: the oblique subduction of the Pacific Plate beneath the Australian Plate along the Hikurangi Trough; oblique right lateral striking structures such as the 650-km long Alpine fault (according to DeMets *et al.* (1994) and Sutherland *et al.* (2006) this fault accommodates 70–75 per cent of the 40 mm yr^{-1} plate motion) and the Marlborough fault zone; the oblique subduction of the Australian Plate beneath the Pacific Plate on the Puysegur Trench. These structures were responsible for all the previous main earthquakes in New Zealand. Despite this, the Canterbury sequence happened in an area (the Canterbury plains) located south of the Marlborough fault zone, that seems to feature different characteristics with respect to the previously described tectonic contest, and characterized in the last years by few low-magnitude earthquakes.

The Christchurch earthquakes is one of the main aftershocks of the Canterbury sequence, which began in 2010 September 4 with the M_w 7.1 Darfield earthquake that occurred in the western part of the Canterbury plains. The magnitude of the Christchurch earthquake (M_w 6.2) was larger than the magnitude of the two previously largest aftershocks, which occurred just some days after the Darfield event, characterized by M_w 4.8 and 4.9, respectively. The Darfield earthquake occurred on the previously unknown 40-km long Greendale fault (Gledhill *et al.* 2011) located about 30 km west of Christchurch. The Christchurch event also occurred in a previously unknown fault under the city of Christchurch. Prior to the Canterbury sequence the region was characterized by a very low-seismicity rate (Bannister *et al.* 2011). The main sources of seismic hazard were the major faults presents and mapped on the Marlborough Fault Zone (see fig. 1 in Elliott *et al.* 2012). Nevertheless, pre-2010 geodetic data indicated that strain was slowly accumulating within the region (Beavan *et al.* 2002; Wallace *et al.* 2007), suggesting the presence of active faults beneath Canterbury (Pettinga *et al.* 2001). However, any potentially active fault would be well hidden beneath the recent Quaternary alluvial deposits (Forsyth *et al.* 2008). Thus, the occurrence of the sequence was in part a surprise.

The Christchurch earthquake was followed by two major aftershocks of M_w 5.8 and 5.9, that occurred within 2 hr of the main shock and located SSW of the main event (Bannister *et al.* 2011). These two events were characterized by a strike-slip focal mechanism. Furthermore, the aftershocks distribution, inferred from the GeoNet catalogue, suggests a prevalent east–west trending (Bannister *et al.* 2011). A further M_w 6.0 aftershock occurred on 2011 June 13, with an epicentre some 5 km further to the ENE. On 2011 December 23 Christchurch was again struck by two large aftershocks, 2 hr apart, of magnitude (M_L) 5.8 and 6.0.

Evidence on the contemporary regional stress field in the central South island (Sibson *et al.* 2011, 2012), were derived mainly from: stress inversion from earthquake focal mechanism, breakout determination from Galleon-1 borehole and strain-rate derived from GPS studies. Results of these analyses suggest a uniform regional stress field on the Canterbury region with maximum compressive stress σ_1 horizontal and oriented WNW–ESE ($\sim 115^\circ$). Similarly, Wallace *et al.* (2007) employed a rotational elastic block model to describe present deformation in the South Island, founding a maximum contraction strain rate oriented $100 \pm 8^\circ$ within the Canterbury/Otago block.

The Canterbury plains is delimited in the southeastern part by the presence of a today extinct Bank Peninsula volcano. Bank Peninsula is the largest accumulation of Miocene volcanism within South Island, New Zealand. Four volcanic groups characterize the volcano: Lyttelton (LVG), Mt Helbert (MHVG), Akaroa (AVG) and Diamond Harbour (DHVG).

INVERSION TECHNIQUE

To invert strong-motion and coseismic displacement data we adopt the approach proposed by Delouis *et al.* (2002). The forward problem for the strong-motion data is solved through the representation theorem (Aki & Richards 2002) written in terms of moment rate assuming that each single subfault, in which the fault plane is discretized, can break only once when it is reached by the propagating rupture front. The Green's functions associated with a simple shear dislocation point source located at the centre of each subfault, are computed, at any station, by the discrete wavenumber method of Bouchon (1981) in a 1-D velocity model. In this way we are able to compute full wavefield synthetic seismograms. For the application to the Christchurch earthquake presented in this paper we used the 1-D velocity model provided for the area under investigation by Reyners & Cowan (1993). The source time function (STF) for each subfault is parametrized according to Nabelek (1984) and it is represented by a set of isosceles triangular time windows of variable height, and mutually overlapping. The number and duration of triangles has to be mainly chosen according to the dominant period of real data. Following this representation of the source, the parameters that are searched through the inversion of strong motion records, or joint seismological—geodetic data, are the rupture onset time, the rake direction, and the amplitude for any of the triangular moment rate functions used.

As for the strong-motion data, even for the GPS and InSAR data the synthetic displacements are obtained through the resolution of the representation theorem. The Green's functions for the static displacement are generated using the formulation of Savage (1980) that considers each subfault as a slipping surface embedded in an elastic half-space. However, the coseismic static displacements are sensitive only to the rake and to the local slip value, not the time history of the rupture. The local slip value can be obtained from the local STF, since the area under the STF is equal to the local seismic moment that is, in turn, related to the local rupture area (known) and

to the slip amplitude. Furthermore, since the InSAR data represent a relative measurement of displacement, the static offset for the InSAR data became another parameter that we explore trough the inversion.

The total cost function (F_{cost}) in the inversion procedure is defined as the sum of two terms. The first one is the weighted (w_j) sum of the rms misfit function, that is, the L_2 norm of observed minus synthetic data, normalized by the observed data (rms_j), for the N_D available data sets. In this case study, we have $N_D = 3$ different data sets corresponding to strong-motion, InSAR, and GPS data. An additional term in the cost function is introduced in order to minimize the total seismic moment of the model moment (Mo_{mod}) taking into account an *a priori* value of seismic moment ($Mo_{\text{a priori}}$). In conclusion, the misfit function is given by

$$F_{\text{cost}} = \frac{\sum_{j=1}^{N_D} \left\{ w_j \left[\sqrt{\sum_{i=1}^{n} (O_i - C_i)^2 / \sum_{i=1}^{n} O_i^2} \right]_j \right\}}{\sum_{j=1}^{N_D} (w_j)} + C_{M_0} e^{\left[\left(\frac{Mo_{\text{mod}}}{Mo_{\text{a priori}}} \right) - 1 \right]},$$

where O_i and C_i represent the real (observed) and synthetic (computed) data, n is the number of data for any data sets and the coefficients C_{Mo} is the weight for the moment constraint. In the application presented in this study we chose to equally weight the three data sets and assumed the seismic moment provided by the GeoNet catalogue (2.24×10^{25} dyne · cm) as *a priori* moment value, with a weighting coefficient of 0.1. This value was chosen in agreement with Delouis *et al.* (2002), who suggest this number on the basis of results from synthetic tests.

For searching the minimum of the cost function, the model space is explored in a quasi-global manner by using the simulated annealing algorithm (Aarts & Korst 1989). However, before performing the inversion, we have to set the investigation ranges for any of the model parameters (i.e. rupture time, rake direction and moment rate).

Moreover, we first invert only the coseismic static displacements associated with InSAR and GPS data to search for the optimal fault orientation and position. We will refer to this step the 'fault inversion'. In the case of Christchurch event, we started fixing the position in space of the fault centre by-eye on the basis of the shape of the SAR's fringes near to the epicentral location area. Then, we searched for the better position (x_c, y_c, z_c) of the fault centre, and strike and dip angles, through the inversion of InSAR and GPS data. In other words, the 'fault inversion' scheme is based on the use of two nested cycles. The external cycle allows for exploring the position and orientation of the fault plane; by using the internal cycle we search for the slip distribution on the fault plane retrieved in the external cycle.

This 'fault inversion' scheme is of course expensive from the computational point of view mainly because for any given fault plane we need to compute the Green's function. However with this approach there is no trade-off between the fault depth and slip amplitude (Beavan *et al.* 2011).

DATA

For the Christchurch earthquake a large amount of data of different nature, such as strong-motion, GPS and SAR data, are available due to the great expansion of the accelerometric and GPS networks following the Darfield earthquake.

Strong-motion data

After the 2010 September 4 Darfield earthquake the New Zealand accelerometric network in the Canterbury plains was supplemented by 13 additional strong-motion stations with CUSP-3 data-logger and triaxial MEMs sensors, by GeoNet network (New Zealand National Hazard Monitoring Network) and its regional component, the CanNet network (Canterbury Network). The Christchurch earthquake was then recorded at 25 stations at epicentral distance between 2 and 50 km. On the basis of some preliminary analysis performed using the fault geometry proposed by Beavan *et al.* (2011) and accounting at the soil conditions (see table 1 in Bradley & Cubrinovski 2011), we decided to use only the 10 strong-motion stations (Fig. 1) located at distances ranging between 2 and 20 km. The selected stations show in any case a good azimuthal coverage. Some of the discarded stations (e.g. ROLC, TPLC and CACS) simply represent a duplication of the selected ones. Moreover, stations like PRPC, SHLC and HPSC are contaminated by strong site effects linked to intense liquefaction phenomena first recognized in the case of the Darfield earthquake (Beavan *et al.* 2010; Palermo *et al.* 2010) so we decided to exclude them from our modelling. However, all recordings used in this study are influenced at some degree by site effects. The Canterbury plains are in fact characterized by very shallow layers inducing non-linear amplifications or trampoline effects (Fry & Gerstenberger 2011). Moreover, as pointed out by Holden (2011), ground conditions within Christchurch are highly variable and will require further studies for stations in this region to be included in the modelling. To choose an appropriate filtering frequency bandwidth, two independent analyses were performed. First, we searched for the frequency range in which the *S*-phase polarization was stable (e.g. Emolo & Zollo 2005; Lucca *et al.* 2012), finding 0.05–0.5 Hz as the optimal frequency range for all the selected records. Then, we performed some preliminary strong-motion inversions in different frequency bands around the limits obtained from the polarization analysis and selecting the range providing the lowest misfit. We found 0.1–0.5 Hz as the best frequency band. Thus, accelerometric data to be used in the inversion were processed removing mean and linear trend, integrated twice and bandpass filtered in the range

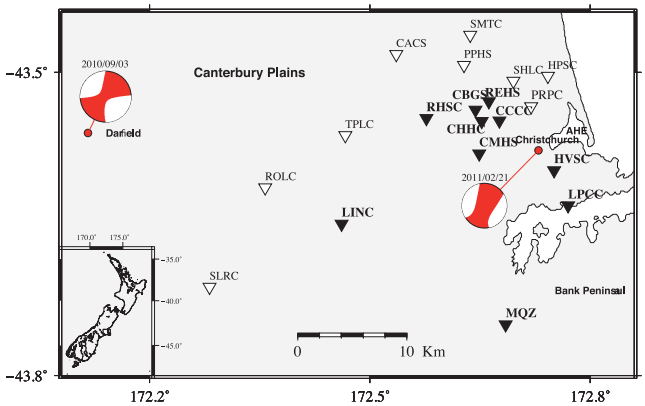

Figure 1. Source–receivers geometry for the Christchurch event. The triangles correspond to the GeoNet (New Zealand National Hazard Monitoring Network) and CanNet (Canterbury Network) strong-motion stations installed in the Canterbury plains. The white and black triangles indicate the discarded and used seismic stations, respectively. Red dots represent the epicentral location for the 2010 September 4, M_w 7.1 Darfield and for the 2011 February 21, M_w 6.2, Christchurch (Bannister *et al.* 2011) earthquake. The focal mechanisms, from the Global Centroid Moment Tensor catalogue, for these two events are also shown in the figure.

0.1–0.5 Hz by a three poles Butterworth filter. The horizontal components from the CanNet stations were also rotated, from their original orientation, to the north–south and east–west orientation. Finally, data were decimated from their original sampling frequency to 2.5 Hz.

InSAR data

The InSAR data used to model the Christchurch earthquake were the same used by Elliott *et al.* (2012), and derived from the Japanese Aerospace Exploration Agency's (JAXA) L-Band ALOS instrument (for all the information related to the two used track we referred to the table 5 of Elliott *et al.* 2012).

The two tracks available for the studied area, that is, tracks 335 (panel a in Fig. 2) and 336 (panel b in Fig. 2), are partially overlapping and cover most of the deformation area around the city of Christchurch. The two ascending interferograms were acquired within the time periods 2011 January 10 to 2011 February 25 (track 335), and 2010 October 27 to 2011 March 4 (track 336). The two longer wavelengths ALOS data (particularly the track 336) show evidence of incoherency in some area on the eastern part of Christchurch city. Nevertheless, coherent fringe coverage is clearly visible just west of the Avon–Heathcote estuary, in particular for the track 335 (panel a in Fig. 2). The fringe shape in this area is of great importance because it could provide information related to the geometry of the rupturing source. The peak displacement along

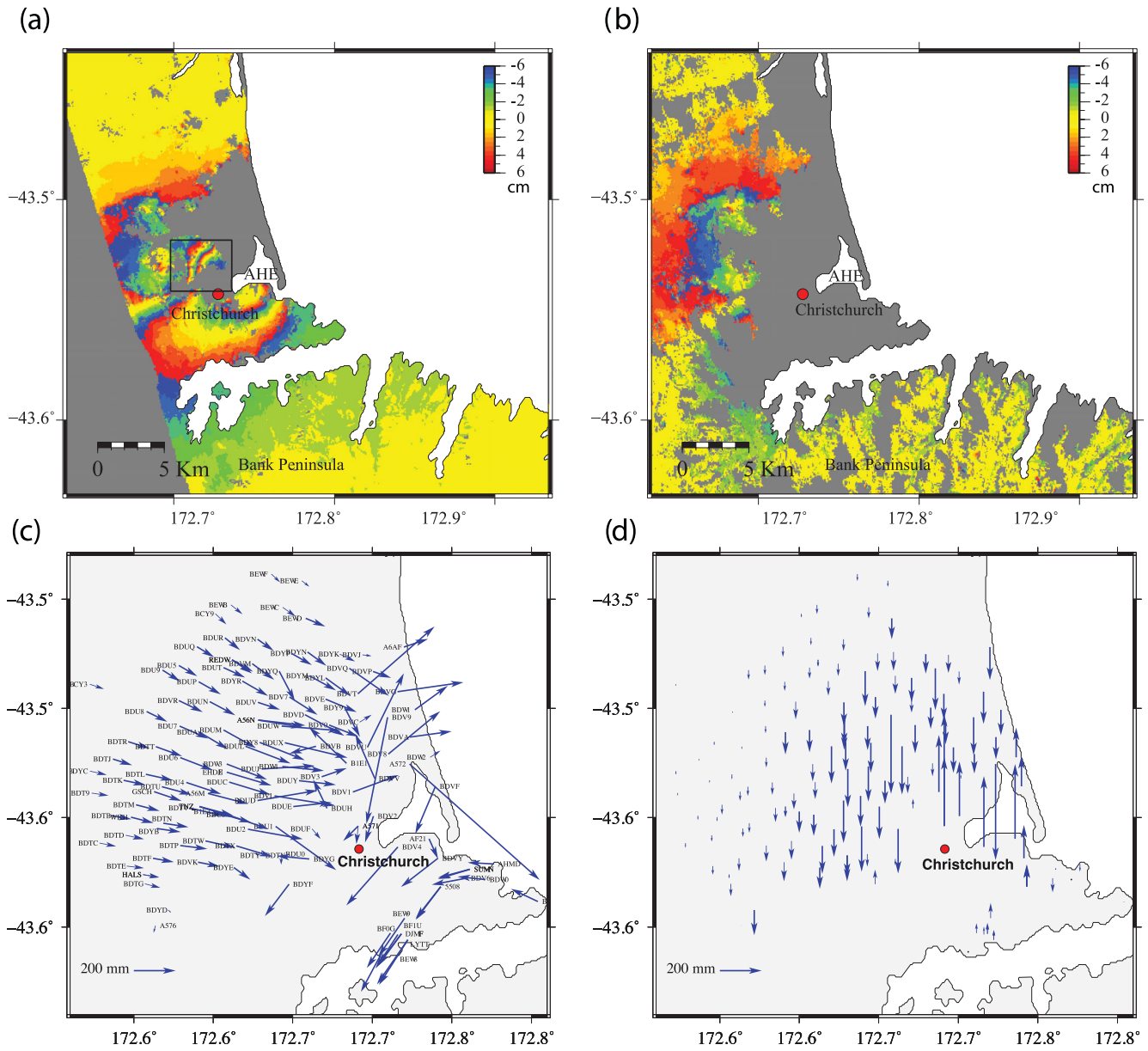

Figure 2. Coseismic geodetic deformation data (InSAR and GPS) for the Christchurch earthquake. Panels a and b show the two ascending interferograms, acquired within the time periods 2011 January 10 to 2011 February 25 (track 335) and 2010 October 27 to 2011 March 4 (track 336), respectively. In panel a, the black box indicates the area, near the Avon–Heathcote estuary (AHE), with the highest complexity of the fringes shape. The panels c and d represent the horizontal and vertical component, respectively, of the GPS sites used in this work. In the Figure, red dots correspond to the epicentral location of the Christchurch earthquake (Bannister *et al.* 2011).

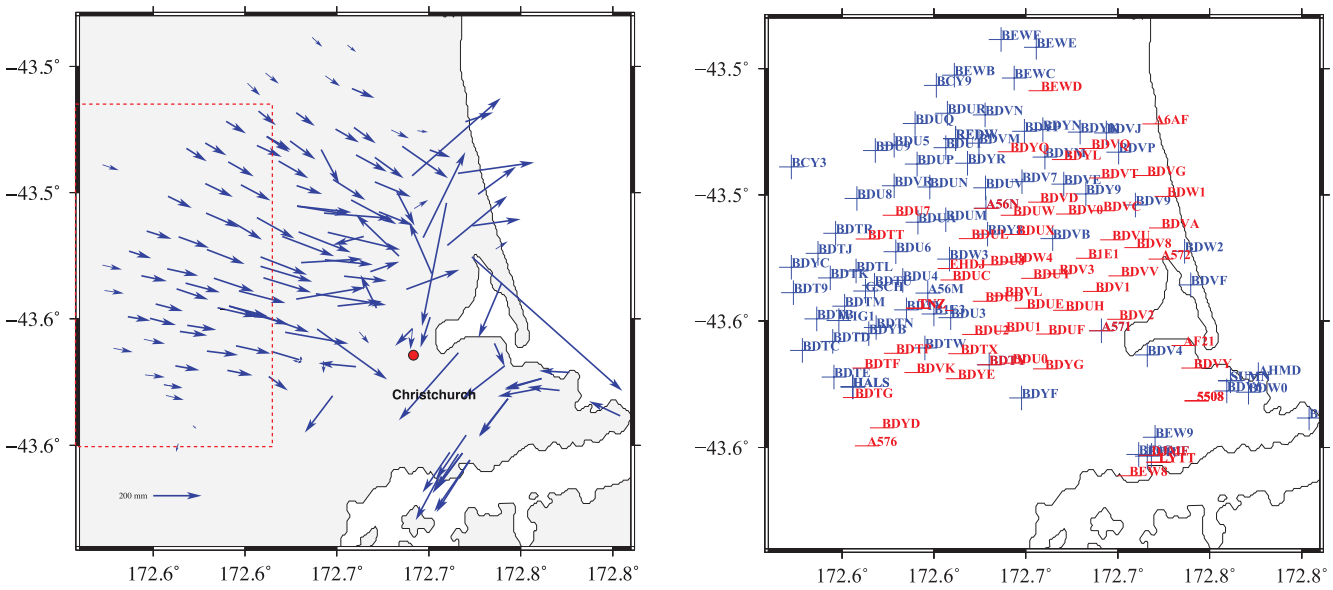

Figure 3. GPS data selection. In the left panel the red box delimitates the GPS sites used to select the GPS data to be used for the inversion (see text for details). The right panel highlights the result of the GPS selection analysis. In this panel the blue and red colours indicate the used and discarded GPS sites, respectively.

the line-of-sight (los) was about 50 cm (towards the satellite) in the south–east area of the city of Christchurch, and about 24 cm around the city centre. For all the information related to the processing of the SAR data we refer to the work of Elliott *et al.* (2012). Two additional tracks from ascending and descending orbit were available for the Christchurch area from the Italian Cosmo-SkyMed (CSK) X-band radar satellite, acquired on 2011February 19 and 23, and 2011 February 20 and 2011 March 16, respectively. However, these data are highly incoherent so we decided to not use them in our modelling.

GPS data

A total of 193 GPS sites are available for the Christchurch earthquake: 57 sites are campaign GPSs collected between the 28 February and the 2011 April 14 following the Darfield earthquake; 5 points are continuous GPS (cGPS) from regional sites of the Land Information New Zealand (LINZ) operated by the GeoNet; 8 are cGPS operated by private companies in the city of Christchurch; and 123 sites are low-accuracy campaign GPSs collected between the 2011 April 14 and the 27. For all the information related to the processing of the GPS data we refer to the work of Beavan *et al.* (2011). To select the GPS sites to be inverted in order to determine the earthquake rupture model, we perform an initial selection based on the epicentral distance of GPS sites. In order to select the sites closest to the epicentral area, we set a threshold distance of 30 km, keeping 132 sites (panels c and d in Fig. 2). Looking at the general trend of the GPS data (panel c in Fig. 2), we notice the presence of some sites (e.g. A572, BDUH, BDUF, and B1E1) having a shape and/or amplitude, especially on the horizontal component, which are not consistent with the general trend highlighted by other GPS. The general trend seems to suggest the presence of a fault plane, having a strike around 60° and characterized by a strike-slip component. Beavan *et al.* (2011) tried to model the outliers increasing the complexity of the model, but they were not able to successfully model these anomalous GPS data. This suggests that these sites were affected by large errors, associated, for instance, with the liquefaction phenomena, rather than being the consequence of a complex rupture model. We tried to model the complete set of data with a two-fault model, without more success. We, therefore, performed a second selection in order to exclude from the data set those data that could be considered as outliers. To this end, we applied the following procedure:

(1) we computed the SAR values, from the more coherent InSAR track (335), over a regular grid centred on the Christchurch earthquake epicentre, using a bicubic spline interpolation, obtaining in this way, the SAR values at the GPS sites;
(2) we projected the three GPS components on the los of the SAR and then computed the difference, at the GPS sites, between the SAR values from the interpolations and the corresponding SAR values obtained from the three GPS components;
(3) using only some selected and considered most reliable GPS sites, we computed the mean value (μ) and the standard deviation (σ) of the SAR differences obtained in the previous step;
(4) we defined the interval [min; max], being min $= \mu - \sigma$ and max $= \mu + \sigma$;
(5) and finally retained only those GPS data inside this range.

The results of this analysis are listed in Fig. 3. To compute the selection interval we chose only the GPS that in some previous analysis showed a surface deformation very similar to that provided by the InSAR data. The corresponding GPS stations are only those reported in the red box in Fig. 3. The results obtained for this study, provide a μ and σ, respectively of about 1.5 and 3 cm, which also provide an indicative estimation of the offset value associated with the InSAR data. Finally, we retain a total of 76 GPS sites for the inversion. Moreover, most of the GPS excluded by this analysis also coincides with the GPS sites with the greatest measuring error (see the GPS table provided by Beavan *et al.* 2011).

INVERSION RESULTS

The strong-motion, InSAR and GPS data selected as described in the previous section constitute the whole data set we used for the inversion.

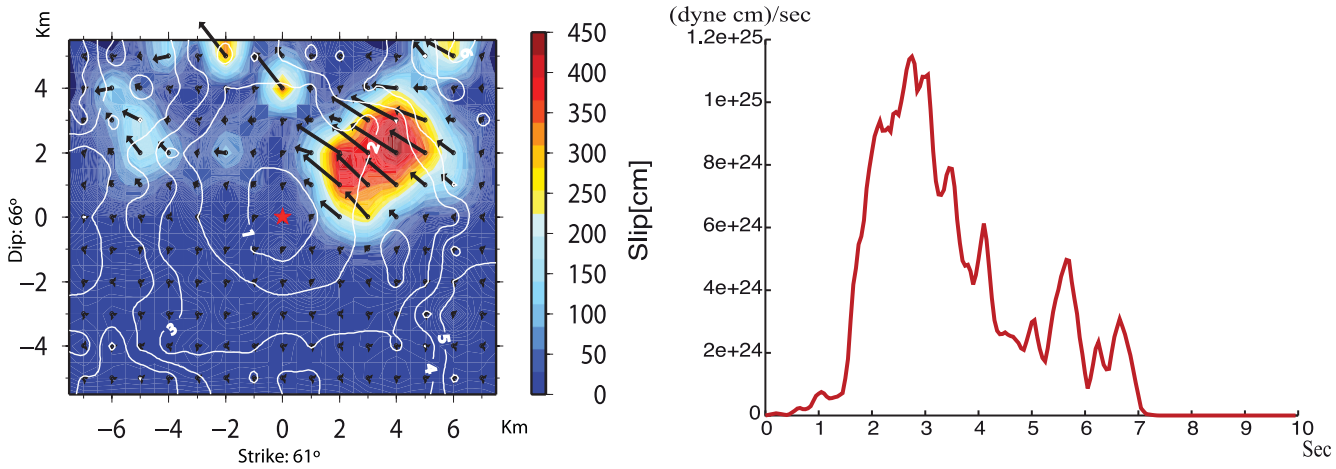

Figure 4. Kinematic rupture model for the Christchurch earthquake. The left panel shows the slip and onset time distribution for the Christchurch event, obtained assuming a single fault plane model from the joint inversion of InSAR, GPS and strong-motion data. The position and geometry of the fault plane has been obtained from the analysis of coseismic geodetic data alone (InSAR and GPS). The black arrows indicate the slip vectors. The right panel shows the global source time function (GSTF) for the obtained slip model.

Following the principle of parsimony, economy or succinctness as set out by the Occam's razor, we first tried to model the Christchurch earthquake using the simplest possible fault model, that is, we started to model the event using a single fault plane. A similar approach was also followed by Beavan *et al.* (2011) and Elliott *et al.* (2012), even if the complex pattern of InSAR and GPS data around the city of Christchurch western of the Avon–Heathcote estuary suggests a more complex model. The same complexity seems also to be required from the moment tensor solutions from seismological catalogues (GeoNet) that shows a large non-double-couple component for this event (Fig. 1).

As described in the 'Method' section, before performing the data inversion to retrieve the kinematic rupture model, we started searching for the geometry of the (single) fault plane to be used as *a priori* information for data inversion. Using the geodetic coseismic information (76 GPS sites and the track 335 for InSAR data), and fixing the fault centre at the hypocentre at position provided by Bannister *et al.* (2011), we obtained a fault plane with a strike of about 61°, dipping towards SE with an angle of 66°, and an average rake of 166°. With this fault geometry we then performed the joint inversion using data from the 10 selected strong-motion stations, the two SAR tracks and the 76 GPS sites. The fault plane has length and width equal to 15 and 11 km, respectively and it is discretized in 1 km^2 subfaults. The local STF of each subfault is represented by three triangular functions of 0.6 s duration with an overlapping of 0.3 s. The maximum allowed duration of slip for a subfault is thus 1.2 s. The results of this inversion are provided in Figs 4–7. The dislocation model that we retrieved (Fig. 4) is characterized by a large patch of slip, localized NE of the hypocentre, with a maximum slip value of about 4.2 m. The average slip on the fault is 0.55 m that corresponds to a seismic moment of about 2.8×10^{25} dyne · cm. The rupture velocity is characterized by a slip weighted average value of 1.9 km s^{-1}. We computed the average rupture velocity weighting the values in each node by the corresponding slip value, in this way we did not include those area of fault plane characterized by low-slip value. The STF has a total duration of about 7 s, and is characterized by 2 main peaks at 3 and 6 s (Fig. 4).

The general fit between real and synthetic data is good for all used data (strong-motion, Fig. 5; GPS, Fig. 6). However, as indicated from the InSAR fringes in Figs 7(c) and (d), the source model derived using a single plane is not able to explain the complexity of the real data in the area west of the Avon–Heathcote estuary. We, therefore, increased the complexity of our model adding a second fault plane.

As for the previous case we first inferred the geometry and position of the two fault planes. Thus, according to the geodetic coseismic data distribution (InSAR and GPS data) we first defined the exploration intervals for the different parameters and then we performed the inversion searching for the strike, dip, average rake and fault centre of the two faults. In particular, the exploration interval for the strike parameter, for the second fault plane included in our modelling was mainly suggested by the curvature in the NNE direction of the InSAR data (track 335). Moreover, while the centre of the largest plane was fixed like in the previous case (single-fault model) at the hypocentre location provided by Bannister *et al.* (2011), the fault centre of the second fault plane was instead explored.

From the inversion of the InSAR and GPS data, we found a first plane having a strike of about 60° and a dip of 68°, results that are very similar to the single-fault model, and characterized by a prevalent strike-slip movement with a small reverse component. The second fault plane has strike and dip equal to 10° and 57°, respectively, and a centre located about 1.5 km northward of the main fault centre, at a depth of 3.7 km and is characterized by a dominant reverse fault style.

To perform the joint strong-motion, GPS and InSAR data inversion for the source kinematics we set the plane dimensions to 15 × 11 km^2 and 7 × 7 km^2, respectively, into 1 × 1 km^2 subfaults. The results of this inversion are provided in Figs 8–13. In particular in Fig. 8 is shown the rupture model obtained from the inversion, here we report the slip distribution, for the strong motion (panel c), GPS (panel a), SAR (panel b) and joint inversion (panel d), over the two fault planes. The main fault plane is characterized by a dislocation pattern very similar to the distribution inferred for the single-fault model. The main patch of slip (maximum slip of about 4.1 m) is again located NE of the hypocentre, while the average slip over the whole fault plane is about 0.5 m. Moreover, an average rake of 150° also characterizes the main plane. The second plane is instead characterized by a lower average slip (about 0.32 m with a maximum value of about 2 m) and shows a main reverse movement (average rake about 90°). The global average slip over both fault

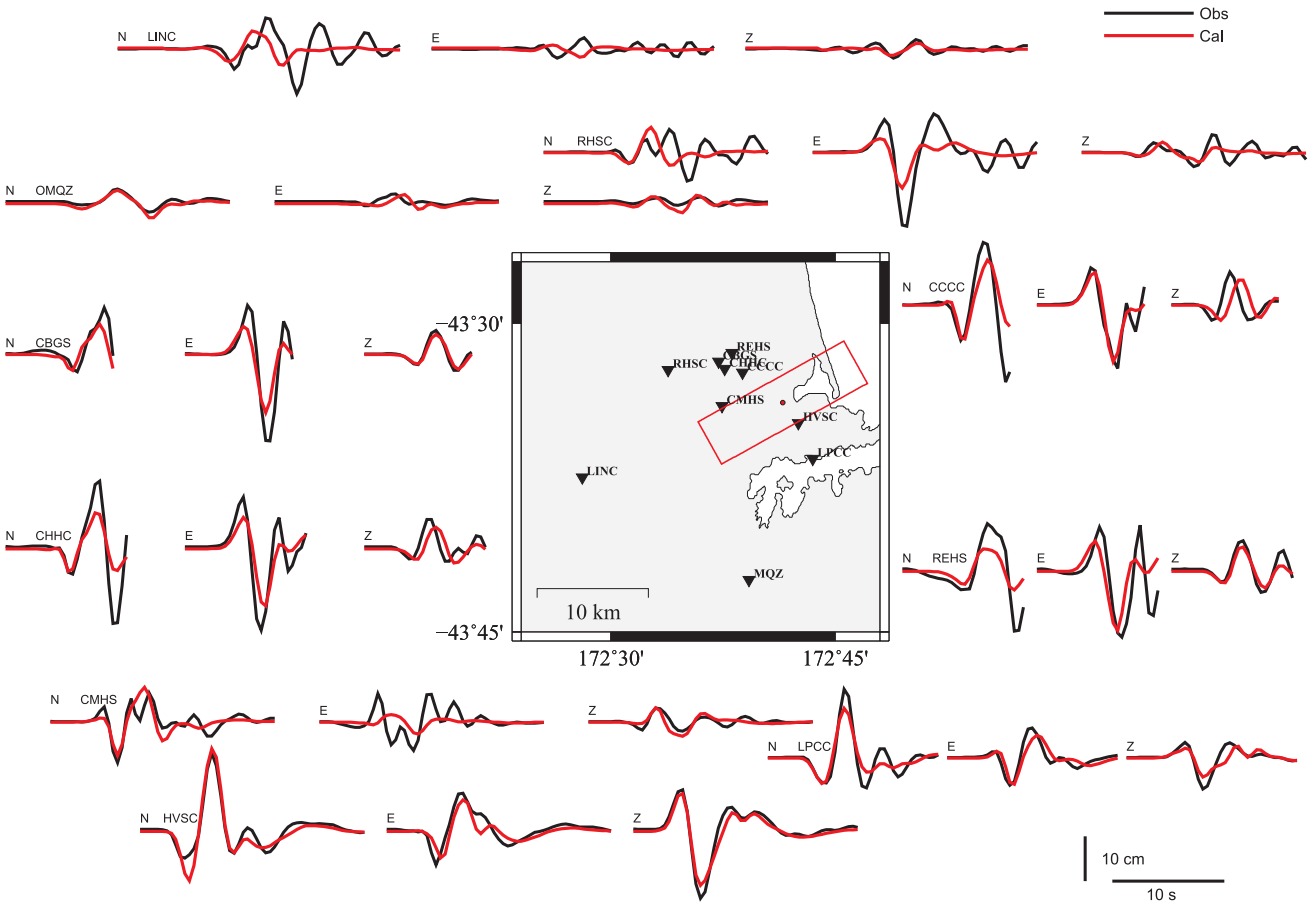

Figure 5. Real (black lines) and synthetic (red lines) computed, for the single-fault model (red box), ground-displacement strong motion records for the north–south, west–east and up–down components, respectively. Data are bandpass filtered in the 0.1–0.5-Hz frequency range. The figure in the middle shows the source–receiver and fault plane geometry used for the strong-motion inversion.

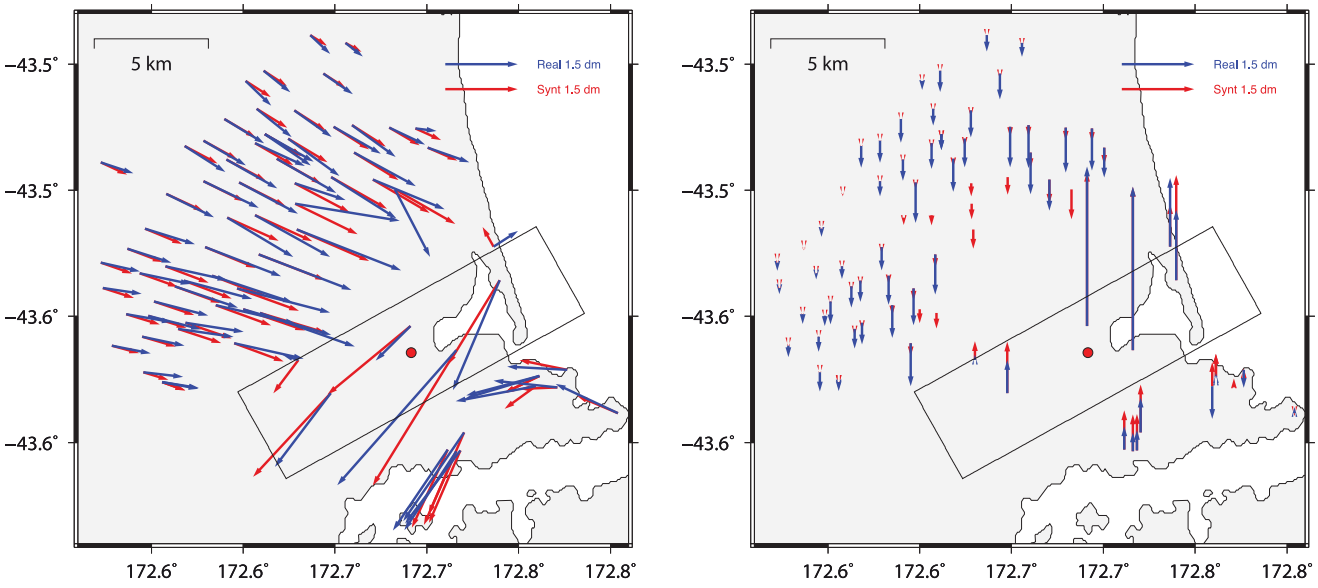

Figure 6. Coseismic GPS vector fitting for the single-fault model. Left panel: observed (blue arrows) and modelled (red arrows) horizontal displacement corresponding to the kinematic rupture model shown in Fig. 4. Right panel: observed (blue arrows) and modelled (red arrows) vertical displacement. The black rectangular frame indicates the fault geometry (projected into the surface), while the red dot is the epicentral location (Bannister *et al.* 2011).

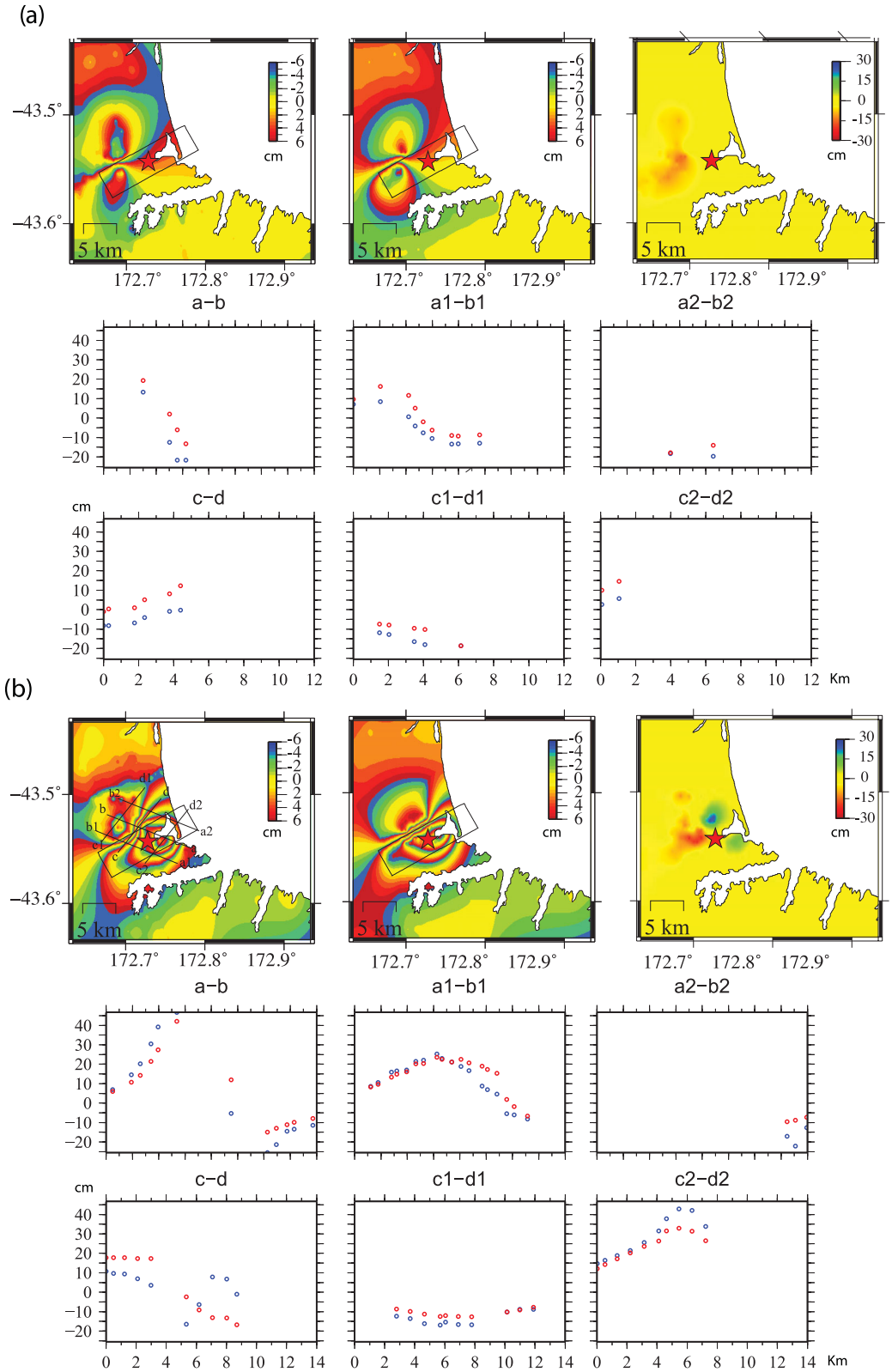

Figure 7. Observed (left), modelled (centre) and residual (right) SAR interferograms based on the single fault plane model, for the Christchurch earthquake. To plot the interferograms we used an interpolation. The panels a and b represent the 336 and 335 used tracks, respectively. Also shown, sections across the interferograms. The location of the sections are shown on the observed interferograms of panel b.

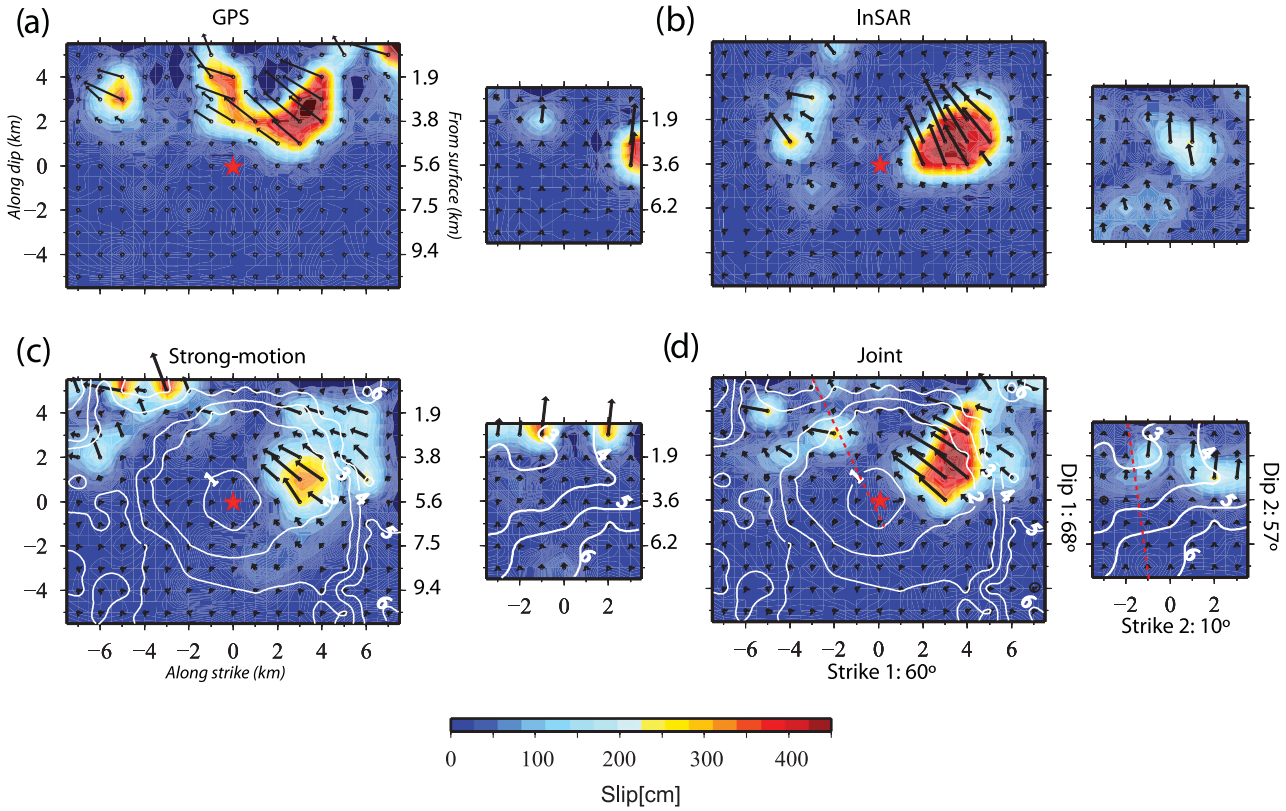

Figure 8. Slip maps from the inversion of real data, for the two-fault model. Panels a, b, c and d display the slip maps for the GPS, InSAR, strong-motion and joint inversions, respectively. The joint inversion combines the three different real data sets. Black arrows indicate the slip vectors. For the joint inversion, we also show the rupture time as contour lines. The red stars represent the hypocentre location on the fault plane. The red dashed lines represents the intersection between the two fault planes.

planes is about 0.45 m corresponding to a seismic moment of about 3.0×10^{25} dyne · cm (i.e. M_w 6.2). Most of slip in our rupture model is concentrated between 2 and 5.5 km depth. This result is in agreement with the lack of superficial evidence of the rupture plane and with the fringe shape, highlighted especially from the track 335.

The rupture velocity on two fault planes has a weighted average slip value of about 1.9 km s^{-1}. Analysing the rupture-time distribution (panel d in Fig. 8), we infer that, on the main fault plane, the rupture front accelerates at the beginning and then slows down. Moreover, the rupture front acceleration was higher on the right-hand side of the fault plane. The rupture duration of the whole faults system lasted about 7 s, like for the single-fault model. This observation indicates that the second fault plane broke at the same time as the first one. In Fig. 9 we provide the snapshots, for the non-335 cumulative (panel a) and cumulative (panel b) slip, at intervals of 0.4 s describing the time evolution of the rupture. It is possible to observe that appreciable values of slip appear 1.6 s after the origin time, while the final slip pattern on the first plane is obtained after 5.2 s. Moreover, the second fault starts contributing to the breakage after about 4 s from the nucleation time. The STF for this model is characterized by the presence of three peaks (Fig. 10), the main of which appears at about 2 s and is associated with the main slip patch. This first peak is very similar, in terms of shape and amplitude, to the main peak of the global STF for the single-fault model. The second peak at about 4 s is instead due to the rupture of the second fault.

Looking at the rupture models obtained from the separate inversions of the single data sets (Fig. 8), we conclude that a second fault plane is required, mostly by the InSAR data. The rms misfit function is markedly improved for the InSAR data, passing from 0.42 for the single fault plane to 0.27 for the two-fault model (see also Fig. 13). Finally, another important result is observed from the residuals analysis on the InSAR data. The introduction of a second fault plane, to model the complex fringe shape near the rupture zone, leads indeed to a clear reduction of the maximum residual value (from 30 cm for the single-fault model to 10 cm for the two-fault model) for both the tracks 335 and 336 (see Figs 7 and 13). We also found an offset of about 0.1 and 0.3 cm for the tracks 335 and 336, respectively; these values are consistent with the expected values from the initial analysis performed with the GPS data (∼1 cm).

We tested the single-fault and the two-fault models both with the restricted (76 stations) and complete (203 stations) GPS data sets, but we did not observe a significant difference in terms of residuals (see Table 1). Another point that needs to be considered is the evaluation of the statistical meaning of models described by a different number of parameters, when the same data sets are used. This study can provide an independent way to choose between the models with one or two fault planes. This analysis is addressed by the corrected Akaike Information Criterion (AICc) for model selection Akaike (1974). This criterion sets that, among various models with different parameter number, we have to choose the one that minimizes the function

$$\mathrm{AICc} = N \ln(2\pi E) + \frac{N(N+P)}{N-P-2},$$

where E represents the misfit value, N the number of data and, finally, P the number of parameters. The minimum of the AICc

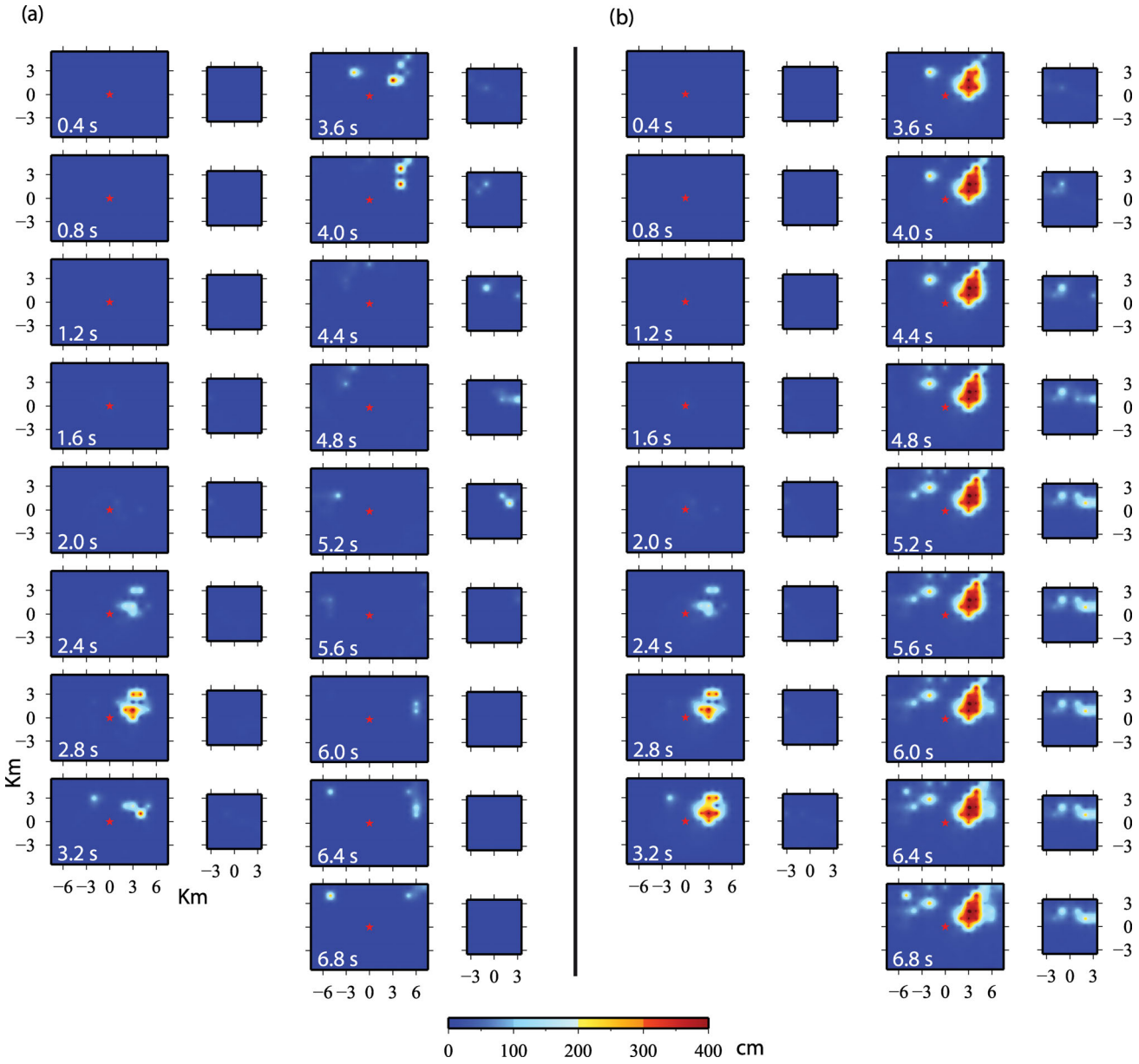

Figure 9. Time evolution of the rupture, for the two-fault model, from the joint inversion of InSAR, GPS and strong-motion data given at intervals of 0.4 s. The left and right panels show the non-cumulative and cumulative slip evolution, respectively. Red stars correspond to the hypocentre location on the fault plane.

corresponds to the best compromise between fit quality and simplicity of the model. The results of the Akaike test show very clearly how the misfit improvement obtained for the geodetic coseismic deformation data, is statistically sufficient to warrant the introduction of the second fault plane, and so for the introduction of a greater number of parameters. The same, however, is not true for the strong-motion data. These results, in any case, can be justified for the narrow frequency band used for the strong-motion data inversion, which is clearly not sufficient to reconstruct the rupture complexity.

RESOLUTION TEST AND ERRORS ANALYSIS

Resolution test

To assess the resolution associated with the different data sets and evaluate the advantages of the joint inversion, we present here the application of the inversion scheme to the synthetic data. This test assesses the performances and limitations of the algorithm and to analyse its spatial and temporal resolution for the real data. For this test we only used the two-fault model and the same data distributions as for the real case.

The synthetic data are generated using the slip distribution shown in Fig. 14, panel a. Four asperities of different shape and dimension (a1, a2, a3, a4), three on the main fault and one on the secondary fault characterize this model. These asperities were located at strategic points of the fault to assess if they are actually resolved by the data. The total seismic moment associated with this slip distribution is equal to 3.0×10^{25} dyne · cm. The rake angle is uniform and set to 110°, a value that represents a good compromise between the two findings obtained for the two fault planes from the inversion of the real data. The rupture velocity is uniform on both planes (2.0 and 1.8 km s^{-1}, respectively) except on the slip patch where the velocity rupture increases to 2.7 km s^{-1}; so we have a total average

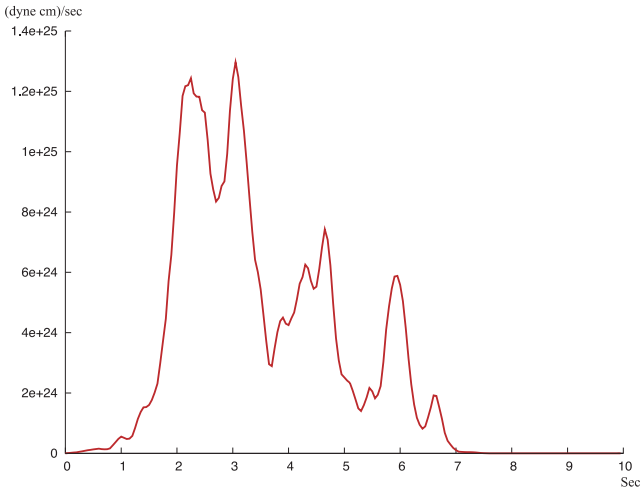

Figure 10. Global source time function (GSTF) for the two-fault plane model obtained from the joint inversion of InSAR, GPS and strong motion data. The GSTF depicts the evolution of the moment rate with time.

rupture velocity over the two fault planes of 2.2 km s^{-1}. Moreover, the rupture initiates at the same hypocentre location as for the inversion of the real data. To generate the synthetic strong-motion and superficial deformation (InSAR and GPS) data we used the discrete wavenumber method of Bouchon (1981) and the analytical solution of Savage (1980), respectively.

We contaminated our synthetic data with uniform random noise into the range ±10 per cent of the amplitude. Fig. 14 (panel b, c, d, e) presents the slip distribution obtained from the inversion of both separate and joint data sets. Concerning the InSAR analysis we performed the joint inversion of the two available tracks (335 and 366). The InSAR data help in defining position and shape of the asperities a1, a2 and a4 (see Fig. 14, panel c), but they are not able to locate the asperity in the deeper part of the main fault. Furthermore, the asperities a1 and a2, which are separated in the initial model, seem to be connected each other in the slip distribution retrieved through the inversion, indicating limitations in the resolution power of these data.

As in the case of the InSAR data, the GPS data identify the asperities a1, a2 and a4 (see Fig. 14, panel b). Again, the shape of the asperities is only approximately retrieved and then also this kind of data has a lower resolution in the lower part of the model. Compared to InSAR however, the shape of the asperities a1 and a2 is better resolved, though the two asperities appear again linked.

The inversion of strong-motion data provides a rupture in which all the asperities are quite correctly identified both for their shape and position (see Fig. 14, panel d). Moreover, the strong-motion data also provide a good resolution of the deepest part of the main

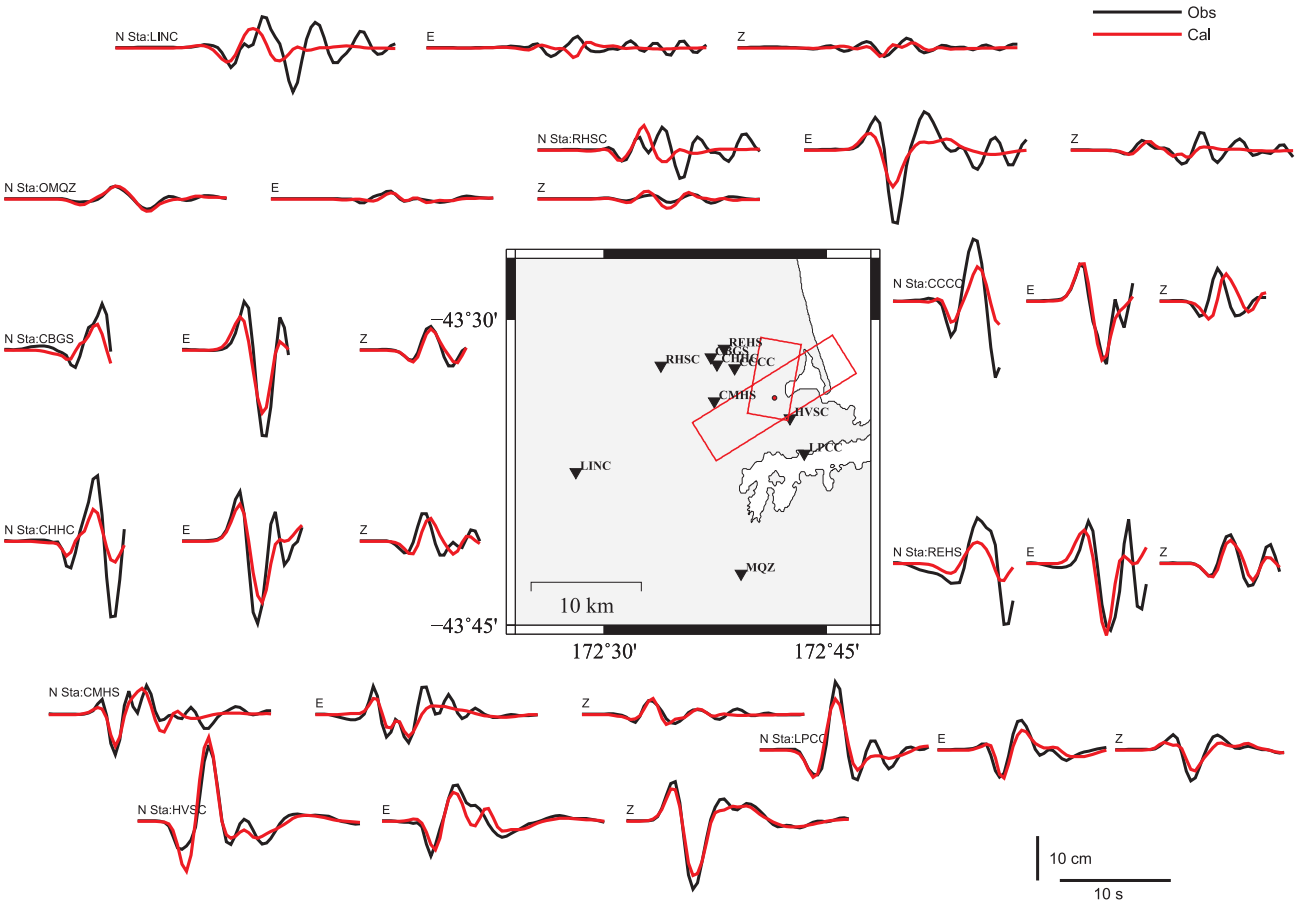

Figure 11. Real (black lines) and synthetic (red lines) computed for the two-fault plane model (red box), ground-displacement strong motion records for the north–south, west–east and up–down component, respectively. Data are bandpass filtered in the 0.1–0.5-Hz frequency range. The panel in the middle shows the source–receiver and the fault plane geometry (surface projection) used for this analysis.

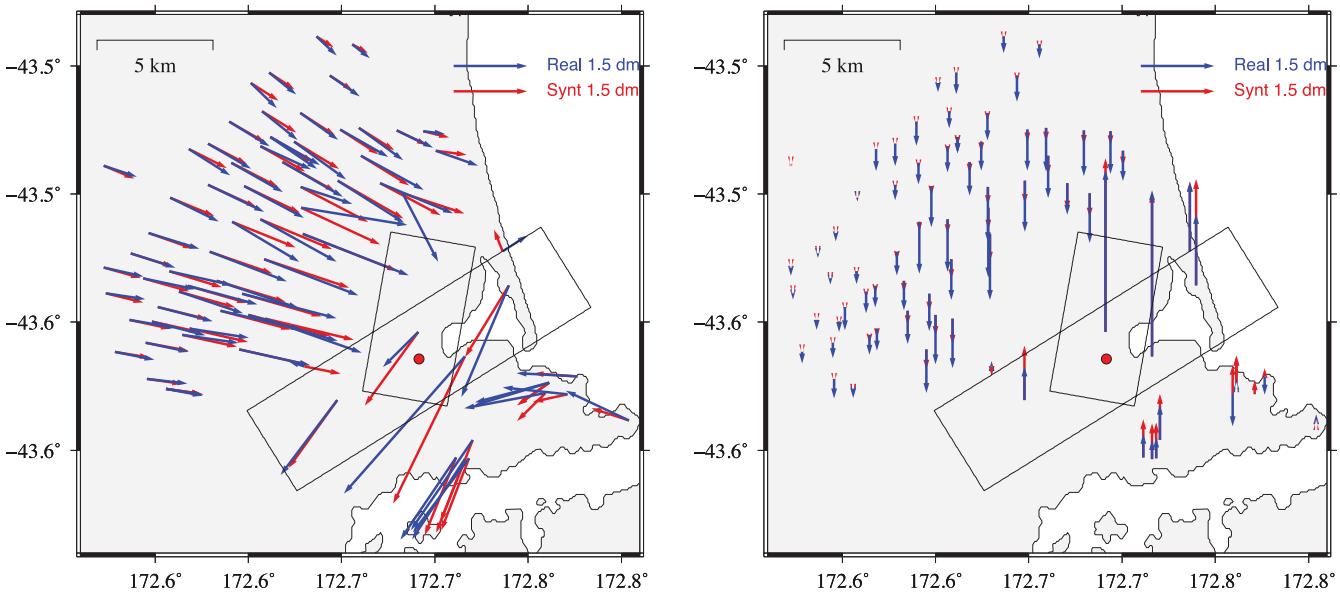

Figure 12. Coseismic GPS vector fitting for the two faults model. Left panel: observed (blue arrows) and modelled (red arrows) horizontal displacement corresponding to the kinematic rupture model shown in Fig. 8, panel d. Right panel: observed (blue arrows) and modelled (red arrows) vertical displacement. The black rectangular frames indicate the fault geometry (surface projection), the red dot the epicentral location (Bannister *et al.* 2011).

fault, which is most likely due to the relative shorter distance of all the stations from the source.

Finally, the joint inversion (see Fig. 14, panel e) of the three data sets shows a very good improvement on the resolution of the initial slip model with respect to the single data sets cases.

It should be noted that the seismic moment inferred from the InSAR, GPS, strong-motion and joint inversions, though in a general good agreement with the starting model, is slightly overestimated. Regarding the rupture velocity, the joint inversion provides an average value of 2.0 km s^{-1}, slightly lower than the average value of the initial model (2.2 km s^{-1}).

The possibility to reproduce quite satisfactorily the position and amplitude of the model asperities using the real data distribution, allows us to suppose that the main features retrieved from the joint inversion of real data are quite well resolved.

Error analysis

We evaluated error estimates on our final model following the approach proposed by Emolo & Zollo (2005). For each subfault we focused one by one on the five parameters defined on it (i.e. rupture time, rake and the three moment values). Fixing all the model parameters at their best values, we perturbed the selected parameter around its best $p_{\rm best}$. Then, for each $p \in [0.9p_{\rm best}; 1.1p_{\rm best}]$ we evaluated the misfit $E(p)$, accounting for all the available data and finally we computed the function

$$\mathrm{pdf}(p) = C\mathrm{e}^{\left[-\frac{E^2(p)}{2\sigma_0^2}\right]},$$

where the normalization constant C is given by

$$C = \frac{1}{\int_{0.9p_{\rm best}}^{1.1p_{\rm best}} \mathrm{e}^{\left[-\frac{E^2(p)}{2\sigma_0^2}\right]}\mathrm{d}p}.$$

In this way the function pdf(p) can be considered as a marginal probability distribution function for the parameter $p_{\rm best}$. The parameter σ_0^2 in the two previous equations is the unknown variance of the misfit function, and accounts for errors both in the modelling and in the data. It determines the shape of the pdf and, in the present case it has to be assigned arbitrarily, according to the best-fitting model variance.

We can characterize these probability distribution functions by their overall widths. One way of measuring the width of a distribution is to multiply it by a function that is zero near the centre of distribution and that grows on each side of centre. The area under the resulting function gives a quantitative measure of the width of the distribution. If one chooses the parabola $(p - p_{\rm best})^2$ as that function, then this area gives the variance σ^2 of the distribution

$$\sigma^2 = \int_{0.9p_{\rm best}}^{1.1p_{\rm best}} (p - p_{\rm best})^2 \mathrm{pdf}(p)\,\mathrm{d}p.$$

According this approach we computed the relative errors for all the model parameters and both for separate and joint data sets. The results of this analysis are shown in the Figs 15 and 16. We generally find a relative error of about 25–30 per cent, with the largest errors associated with the rupture times. This last result is consistent with the slight underestimation on the velocity rupture we found from the resolution test.

DISCUSSION OF RESULTS

The Canterbury plains over the last 2 yr have been characterized by two main seismic events: the 2010 September 4, M_w 7.1 Darfields earthquake and the 2011 February 21, M_w 6.2 Christchurch earthquake. The latter occurred in an area characterized by a large aftershocks activity related to the Darfield earthquake and by an increase of the Coulomb static stress induced by the previous earthquake, suggesting that the Darfield earthquake may somehow have influenced the occurrence of the Christchurch event (Zhan *et al.* 2011).

A large quantity of data of different nature, that is, InSAR, GPS and strong-motion data, are available to study the source model of the Christchurch earthquake. In particular, the coseismic geodetic data suggest a complex geometry for the source, as in the case of the Darfield event (Elliott *et al.* 2012) that occurred in the western part of the Canterbury plains.

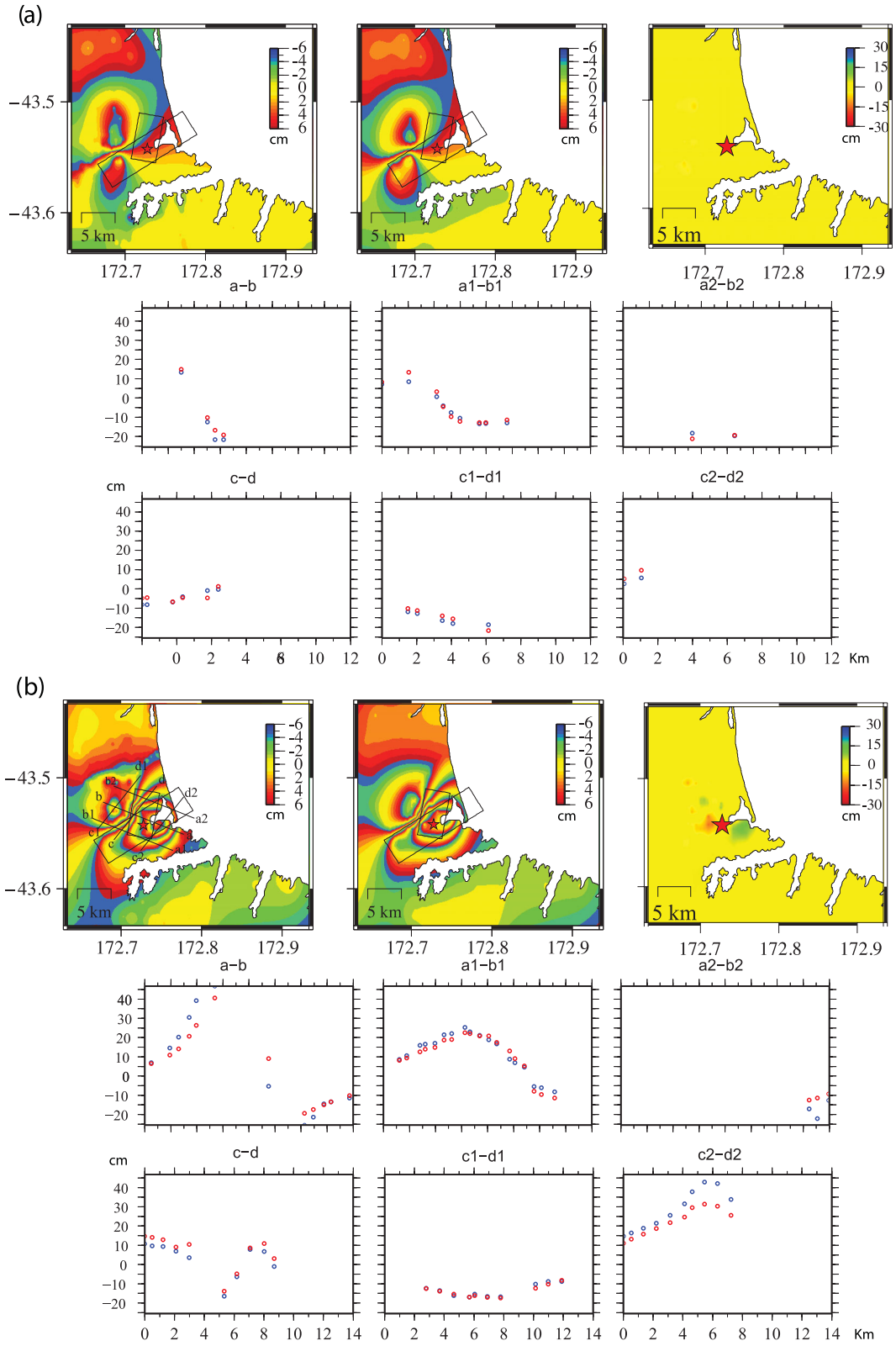

Figure 13. Observed (left), modelled (centre) and residual (right) SAR interferograms based on the two-fault plane model, for the Christchurch earthquake. The panels a and b represent the 336 and 335 used tracks, respectively. Also shown, sections across the interferograms. The location of the sections are shown on the observed interferograms of panel b.

Table 1. Fault model parameters and normalized rms misfit values from our inversions. In the table we report the different rms values obtained from the inversion of the different separate data sets [InSAR, GPS and Strong-motion as well as that from the joint inversion (Joint)]. Results are listed for the two source models studied in this paper. Moreover, for the GPS data two different cases, corresponding to the 76 selected GPS stations and to the complete data set, are reported. The joint rms is obtained combining InSAR, strong-motion and selected GPS data. We also reported the comparison between the fault geometries retrieved in our work and that obtained in other works. Finally in the last column we show the Akaike value corresponding to the used fault models (Akaike values not present on my version).

	My model strike/dip/rake (degree)	Beavan *et al.* (2011)	Barnhart *et al.* (2011)	Beavan *et al.* (2012)	Elliott *et al.* (2012)	Atzori *et al.* (2012)	GeoNet	InSAR	GPS (76)	GPS (203)	St. Mo	Joint	Akaike
1-Fault model	61/66/150	59/66.5/	57/60/64	–	–	–	55/66/129	0.42	0.39	0.77	0.62	0.59	
2-Fault model	60/68/150 10/57/90	58/72/RL 79.5/87/Rev	–	–	70/69/164 27/59/101	70/70/−173 30/60/100	–	0.27	0.35	0.72	0.61	0.53	
3-Fault model	–	–	–	67/70/RL 15/75/Rev 64/70/Rev	–	–	–	–	–	–	–	–	

We used the non-linear inversion method proposed by Delouis *et al.* (2002) to invert the available data sets in order to determine the geometry of the fault plane(s) and the kinematic features of the seismic source for the Christchurch event.

Adopting a single-fault model, we found a plane striking N59° and with a dip angle of 66°. This result is consistent with the inferences obtained by Beavan *et al.* (2011) (strike = 59° and dip = 66.5°) analysing the GPS data and by Barnhart *et al.* (2011) (strike = 59° and dip = 64°). The faulting mechanism is prevalently strike-slip with a small reverse component (average rake = 150°), quite consistent with the solution reported in the catalogue GCMT. On the other hand, our solution differs, mainly for the rake value, from the mechanism in the GeoNet catalogue. Our average rake angle is consistent with that founded by Beavan *et al.* (2011) but is different to that by Barnhart *et al.* 2011 (∼70°).

The kinematic rupture model found in this study is very similar to those provided by Beavan *et al.* (2011) and Barnhart *et al.* (2011) and it is characterized by a main slip patch located NE of the hypocentre. Compared to Beavan *et al.* (2011) and Barnhart *et al.* (2011) models, however, our model presents a much more localized slip patch characterized by a maximum slip value of about 4.3 m, larger than the 2.5 m found by Beavan *et al.* (2011) and 2.1 m found by Barnhart *et al.* (2011). Our maximum value of 4.3 m is in any case very close to that retrieved by Holden (2011), 4.2 m, inferred from the inversion of the strong-motion data.

Compared to the Holden (2011) kinematic model, which prescribes a total rupture duration of about 4 s, we found a lower average rupture velocity, which leads us to have a total duration of the rupture of about 7 s.

Then, we moved to consider a more complex fault model as also done by Beavan *et al.* (2011), Elliott *et al.* (2012), Beavan *et al.* (2012) and Atzori *et al.* (2012). Our geometries, retrieved from the inversion of InSAR data, are quite different from the two fault models proposed in previous studies even if they share some features with both already published models.

In particular, while our main plane is similar to that of Beavan *et al.* (2011), the two models completely differ for the second plane. In fact, the second plane by Beavan *et al.* (2011) is characterized by a strike-slip mechanism and is located south of the main plane (in this work the position of the second fault plane was obtained from the aftershocks distribution), while in our model the second plane is located north of the first and is mainly associated with a reverse mechanism. On the other hand, our model is similar to those proposed by Elliott *et al.* (2012) and Atzori *et al.* (2012) who studied the InSAR data. These models share a quite similar geometry with two planes having different strike, the more north–south strike fault plane characterized by a dominant reverse movement and the more east–west strike plane with a mainly strike-slip mechanism. The two models strongly differ for the slip distribution. In fact, the Elliott *et al.* (2012) and Atzori *et al.* (2012) rupture models prescribe the large part of the total seismic moment as associated with the reverse fault plane with the more north–south strike while in our model, most of the seismic moment is instead associated with the fault plane having more east–west strike and strike-slip mechanism.

Compared to the fault geometry proposed in Beavan *et al.* (2011) in a following work (Beavan *et al.* 2012), the authors introduced in their model a third fault plane located north of the main fault plane. This fault plane shows a good agreement in geometry, position and mechanism with our northern segment. The possibility of introducing a third fault plane more to the south was also investigated in this work, but was rejected because it did not produce any improvement in the misfit compared with the two-fault models, for all of the used data set. On the other hand, Beavan *et al.* (2011) already noted that their second segment, located south of the main one, did not lead to any statistically significant improvements of the data fit.

Concluding, we found that the addition of the second fault plane in the north, with dominant reverse motion, in our model for the Christchurch earthquake, leads to a marked improvement in the fit of the InSAR data (track 335), even if it does not provide a substantial improvement in fit for the strong motion and GPS data. This second fault plane, however, allows us to reproduce some complex shape of the InSAR fringes that cannot be explained by a single fault model. In other words, the InSAR data require the two-fault solution, while the strong motion data are pretty well reproduced by just the main fault. Finally, it should also be highlighted how the introduction of the second fault plane in any case does not lead to a degradation of the rms for both the GPS and strong-motion data. Anyway, we performed a forward modelling of ground-motion in order to check if our complex source model (i.e. the two-fault plane model) was able to reproduce the high shaking value that characterized the Christchurch earthquake. To this aim, we computed synthetic accelerations at a maximum frequency of 10 Hz at different stations located both in the footwall (e.g. CCCC and RHSC) and hangingwall (e.g. HVSC and LPCC). Results of these analysis show that our rupture model allows to well reproduce the spatial distribution (characterized by lower—about 0.2 g—and higher—about

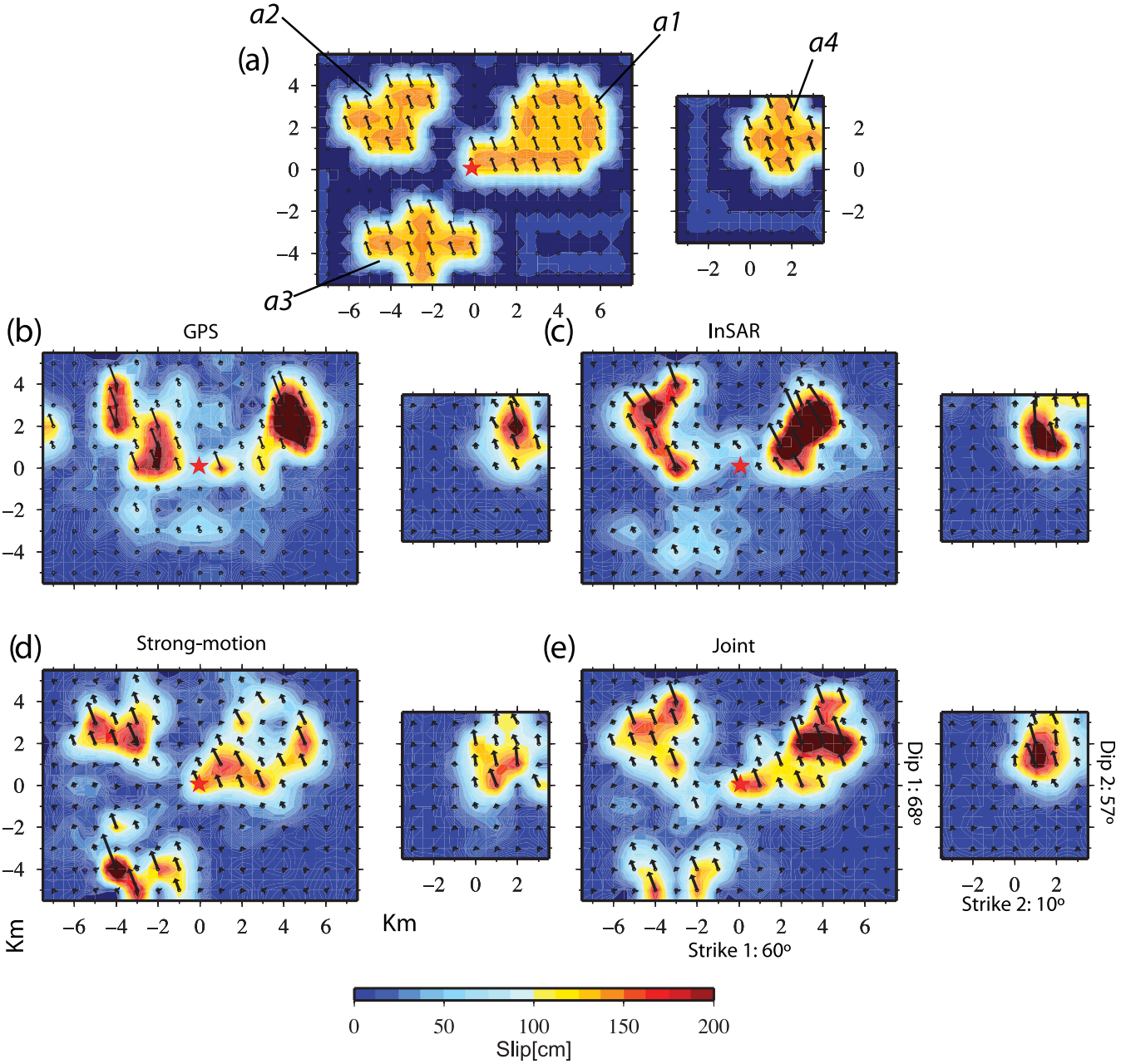

Figure 14. Slip maps from the resolution tests. Panels a, b, c, d and e correspond to the slip maps for the synthetic model (two fault planes), and then for the GPS, InSAR, strong-motion and joint inversions, respectively. The joint inversion combines the three different synthetic data sets. The black arrows indicate the slip vectors, while the red star represents the hypocentre location.

0.9 g–values generally localized in the west and east side of the Christchurch city, respectively), and amplitude of the PGAs, even if slight PGA underestimation is retrieved at the HVSC station. This can be ascribed to the site effects not accounted in our simulations, which are recognized to have strongly influenced the strong-motion data producing, especially at high frequency, local strong amplification (Bradley & Cubrinovski 2011).

Finally, we also evaluated a stress-drop of 4.5 and 5.3 MPa for the main and second fault plane, respectively, using the Madariaga (1977) formulation and considering only the fault portions characterized by significantly non-zero slip.

Furthermore, another point that seems to endorse the choice of a complex fault geometry for the Christchurch earthquake is that the Darfield earthquake is also characterized by a complex faulting geometry with the alternation of planes having different strike and whose mechanism changes from strike-slip to reverse (Atzori *et al.* 2012; Beavan *et al.* 2012; Elliott *et al.* 2012).

CONCLUSIONS

A complex shape of the earthquake source seems to characterize all the main events of the Canterbury sequence. Nevertheless, as discussed in the previous sections, the very low-seismicity rate before the Canterbury sequence, jointly with the lack of superficial evidence of possible deep rupture (associated with the

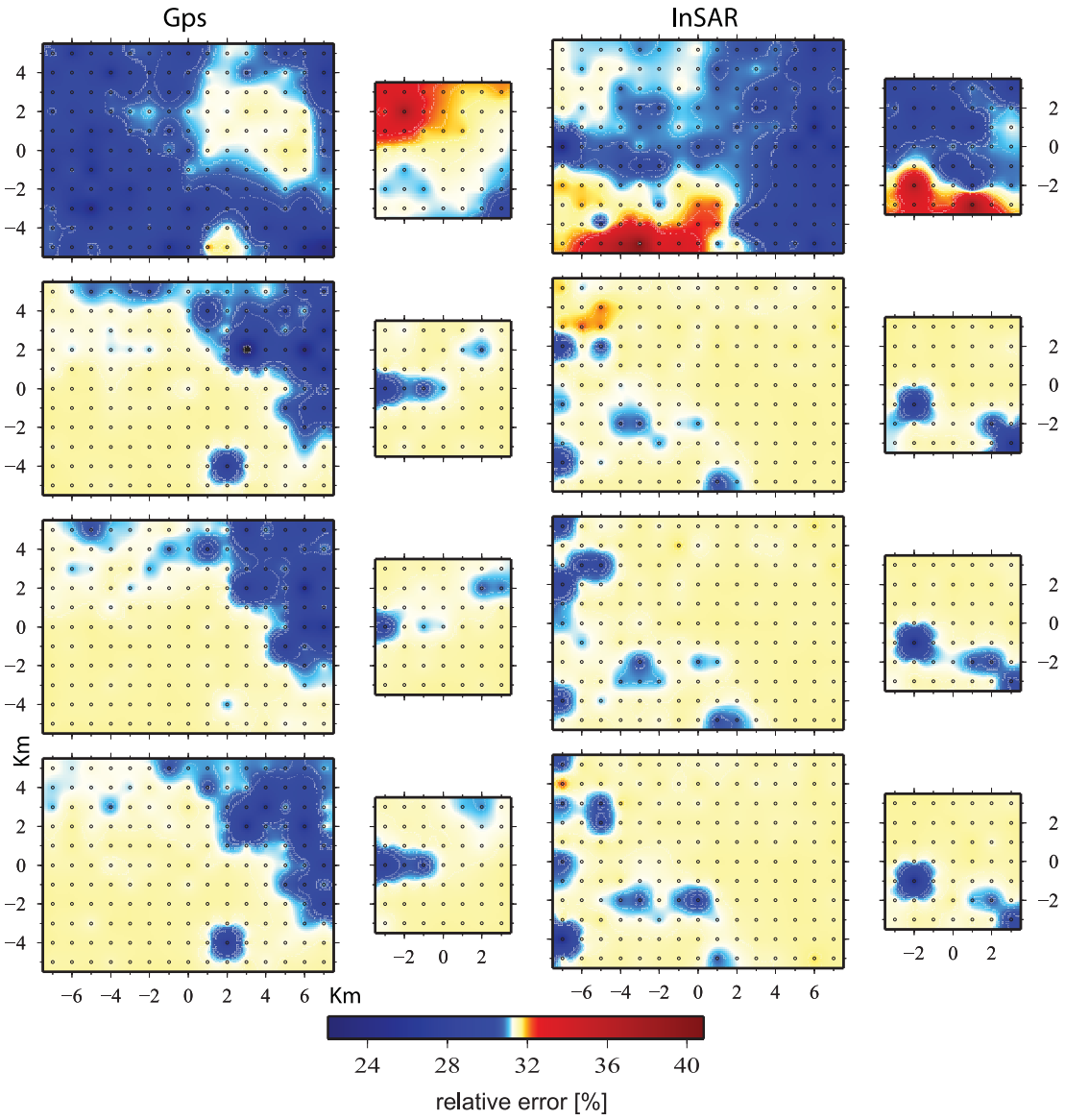

Figure 15. Relative error distributions for the InSAR (left) and GPS (right) data inversions. From the top to the bottom are displayed the relative errors for the slip vector and for the three moment values, corresponding to the three triangular functions whereby we discretized any local source time function.

thick alluvial sedimentary layer) did not allow us, before the beginning of the sequence, to expect such a complex faulting process. Of course, it could be driven by a possible reactivation of pre-existing complex structures (e.g. associated with the intrusion of the Bank Peninsula Volcano) that could play an important role.

Finally, the geometry and source model for the Christchurch earthquake retrieved in this work well fit with the regional stress field actually present in the Canterbury plains and characterized by a maximum contraction axis σ_1 of 100°–115° (Wallace *et al.* 2007; Sibson *et al.* 2011). From this point of view a key role, however, has the uncertainty orientation of σ_3 axes. Indeed if the predominant strike-slip events seem to suggest a horizontal σ_3 axis, the simultaneous presence of inverse events in the Canterbury area, may indicate local variation of σ_3. Furthermore, considering the mixture of strike-slip and reverse faulting during the entire Canterbury sequence, it seems likely that the stress field is of the form $\sigma_1 > \sigma_v = \sigma_2 \sim \sigma_3$ with local variance between $\sigma_v = \sigma_2$ and $\sigma_v = \sigma_3$.

Therefore, considering this, we hypothesize that orientations and mechanisms (150° and 90° for southern and northern segments, respectively) of two fault planes used to modelled the Christchurch earthquake are associated to a local rotation from horizontal plane of the σ_3 axes. As suggested also from other authors (Barnhart *et al.* 2011; Holden 2011; Sibson *et al.* 2011) it is possible that perturbation of local stress in the Christchurch area, could be driven always by the presence of the Banks Peninsula volcano south of the Canterbury plains.

ACKNOWLEDGEMENTS

Our gratitude goes to J. R. Elliott for having provided the InSAR data and to C. Holden for having provided the strong-motion data. We also thank Saskia Goes and two anonymous reviewers for their constructive comments that lead to a great improvement of our work. The figures in this article were made with Generic Mapping Tools (Wessel & Smith 1998).

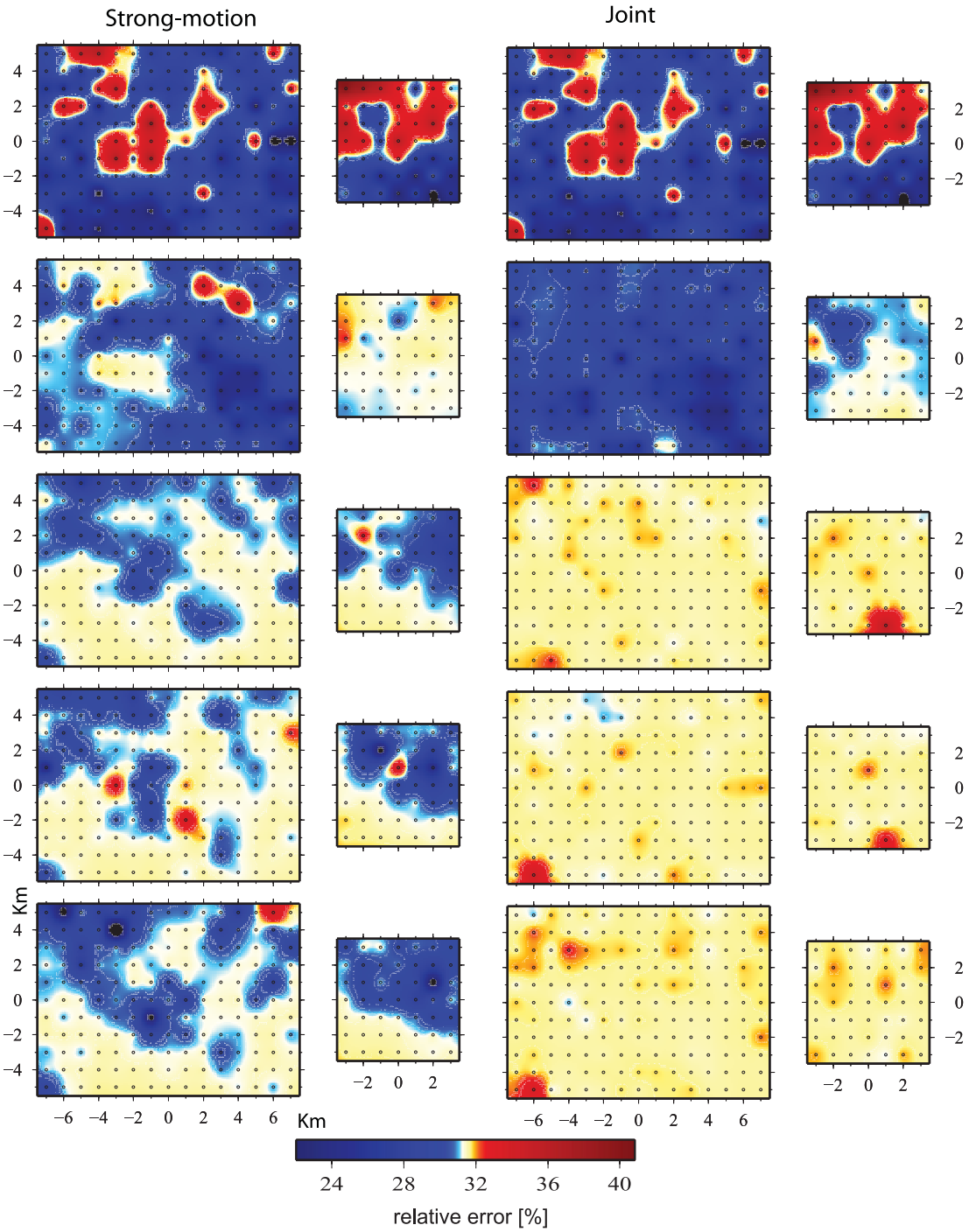

Figure 16. Relative error distributions for the strong-motion data (left) and joint (right) inversions. From the top to the bottom are displayed the relative errors for the onset-time, slip vector and for the three moment values, corresponding to the three triangular functions whereby we discretized any local source time function.

REFERENCES

Aarts, E. & Korst, J., 1989. *Simulated Annealing and Boltzmann Machines: A Stochastic Approach to Combinatorial Optimization and Neural Computing,* Wiley, New York.

Akaike, H., 1974. A new look at the statistical model identification, *IEEE Trans. Autom. Control,* **6,** 716–723.

Aki, K. & Richards, P.G., 2002. *Quantitative Seismology,* 2nd edn, University Science Books Sausalito, California.

Atzori, S., Tolomei, C., Antonioli, A., Merryman Boncori, J.P., Bannister, S., Trasatti, E., Pasquali, P. & Salvi, S., 2012. The 2010–2011 Canterbury, New Zealand, seismic sequence: multiple source analysis from InSAR data and modeling, *J. geophys. Res.,* **117,** B08305, doi:10.1029/2012JB009178.

Bannister, S., Fry, B., Reyners, M., Ristau, J. & Zhang, H., 2011. Fine-scale relocation of aftershocks of the 22 february mw 6.2 christchurch earthquake using double-difference tomography, *Seism. Res. Lett.,* **82,** 839–845.

Barnhart, W.D., Willis, M.J., Lohman, R.B. & Melkonian, A.K., 2011. InSAR and Optical Constraints on Fault Slip during the 2010–2011 new Zealand earthquake sequence, *Seism. Res. Lett.,* **82,** 815–823.

Beavan, J., Tregoning, P., Bevis, M., Kato, T. & Meertens, C., 2002. Motion and rigidity of the Pacific plate and implications for plate boundary deformation, *J. geophys. Res.,* **107,** 2261–2276.

Beavan, J., Samsonov, S., Motagh, M., Wallace, L., Ellis, S. & Palmer, N., 2010. The Mw 7.1 Darfield (Canterbury) Earthquake: geodetic observations and preliminary source model, *Bull. N. Zeal. Soc. Earthq. Eng.,* **43,** 228–235.

Beavan, J., Fielding, E., Motagh, M., Samsonov, S. & Donnelly, N., 2011. Fault location and slip distribution of the 22 February 2011 Mw 6.2 Christchurch, New Zealand, earthquake from geodetic data, *Seism. Res. Lett.,* **82,** 789–799.

Beavan, J., Motagh, M., Fielding, E.J., Donelly, N. & Collett, D., 2012. Fault slip models of the 2010–2011 Canterbury, New Zealand, earthquakes from geodetic data and observations of postseismic ground deformation, *New Zealand J. Geol. Geophys.,* **55,** 207–221.

Bouchon, M., 1981. A simple method to calculate Green's functions for elastic layered media, *Bull. seism. Soc. Am.,* **71,** 959–971.

Bradley, A.B. & Cubrinovski, M., 2011. Near-source stron ground motions observed in the 22 February 2011 Christchurch Earthquake, *Seism. Res. Lett.,* **82,** 853–865.

Delouis, B., Giardini, D., Lundgren, P. & Salichon, J., 2002. Joint inversion of InSAR, GPS, teleseismic and strong motion data for the spatial and temporal distribution of earthquake slip: application to the 1999 Izmit mainshock, *Bull. seism. Soc. Am.,* **92,** 278–299.

DeMets, C., Gordon, R.G., Argus, D.F. & Stein, S., 1994. Effect of recent revisions to the geomagnetic time scale on estimates of current plate motion, *Geophys. Res. Lett.,* **21,** 2191–2194.

Elliott, J.R., Nissen, E.K., England, P.C., Jackson, J.A., Lamb, S., Li, Z., Oehlers, M. & Parsons, B., 2012. Slip in the 2010–2011 Canterbury earthquakes, New Zealand, *J. geophys. Res.,* **117,** B03401, doi:10.1029/2011JB008868.

Emolo, A. & Zollo, A., 2005. Kinematic source parameters for the 1989 Loma Prieta earthquake from the nonlinear inversion of accelerograms, *Bull. seism. Soc. Am.,* **95,** 981–994.

Forsyth, P.J., Barrell, D.J.A. & Jongens, R., 2008. *Geology of the Christchurch area, 1:250,000 Geological Map 16,* Institue of Geological and Nuclear Sciences, GNS Science, Lower Hutt, New Zealand.

Fry, B. & Gerstenberger, M., 2011. Large apparent stresses from the Canterbury earthquakes of 2010 and 2011, *Seism. Res. Lett.,* **82,** 833–838.

Gledhill, K., Ristau, J., Reyners, M., Fry, B. & Holden, C., 2011. The Darfield (Canterbury, New Zealand) Mw 7.1 Earthquake of September 2010: a preliminary seismological report, *Seism. Res. Lett.,* **82,** 378–386.

Holden, C., 2011. Kinematic source model of the 22 February 2011 Mw 6.2 Christchurch earthquake using strong motion data, *Seism. Res. Lett.,* **82,** 783–788.

Kaiser, A. *et al.*, 2012. The Mw 6.2 Christchurch earthquake of February 2011: preliminary report, *New Zealand J. Geol. Geophys.,* **55,** 67–90.

Lucca, E., Festa, G. & Emolo, A., 2012. Kinematic inversion of strong-motion using a Gaussian parameterization for the slip: application to the 2008 Iwate-Miyagi, Japan, earthquake, *Bull. seism. Soc. Am.,* **102,** 2685–2703.

Madariaga, R., 1977. Implications of stress-drop models of earthquakes for the inversion of stress drop from seismic observations, *Pure Appl. Geophys.,* **115,** 301–316.

Nabelek, J., 1984. Determination of earthquake fault parameters from inversion of bodywaves, *PhD thesis,* MIT, Cambridge, MA, pp. 361.

Palermo, A., Le Heux, M., Bruneau, M., Anagnostopoulou, M., Wotherspoon, L. & Hogan, L., 2010. Preliminary findings on performance of bridges in the 2010 Darfield earthquake, *Bull. N. Zeal. Soc. Earthq. Eng.,* **43,** 412–420.

Pettinga, J.R., Yetton, M.D., Van Dissen, R.J. & Downes, G.L., 2001. Earthquake source identification and characterisation for the Canterbury region, South Island, New Zealand, *Bull. N. Zeal. Soc Earthq. Eng.,* **34**(4), 282–317.

Reyners, M.E. & Cowan, H., 1993. The transition from subduction to continental collision: crustal structure in the north Canterbury region, New Zealand, *Geophys. J. Int.,* **115**(3), 1124–1136.

Savage, J.C., 1980. Dislocations in seismology, in *Dislocations in Solids,* ed. Navarro, F.R.N., North-Holland, New York.

Sibson, R., Ghisetti, F. & Ristau, J., 2011. Stress control of an evolving strike-slip fault sustem during the 2010–2011 Canterbury, New Zealand, earthquake sequence, *Seism. Res. Lett.,* **82,** 824–832.

Sibson, R.H., Ghisetti, F.C. & Crookbain, R.A., 2012. Andersonian wrench faulting in a regional stress field during the 2012–2011 Canterbury, New Zealand, earthquake sequence, *Geol. Soc., Lond., Spec. Publ. 2012,* **367,** 7–18.

Sutherland, R., Berryman, K. & Norris, R., 2006. Quaternary slip rate and geomorphology of the Alpine fault: implications for kinematics and seismic hazard in southwest New Zealand, *Bull. geol. Soc. Am.,* **118,** 464–474.

Wallace, L., Beavan, J., McCaffrey, R., Berryman, K.R. & Denys, P., 2007. Balancing the plate motion budget in the South Island, New Zealand, using GPS, geological and seismological data, *Geophys. J. Int.,* **168,** 332–352.

Wessel, P. & Smith, W.H., 1998. New, improved version of generic mapping tools released, *EOS Trans. AGU,* **79,** 579.

Zhan, Z., Jin, B., Wei, S. & Graves, W., 2011. Coulom stress change sensitivity due to variability in mainshock source models and receiving fault parameters: a case study of the 2010–2011 Christchurch, New Zealand earthquake, *Seism. Res. Lett.,* **82,** 800–814.